Materials Advances

ROYAL SOCIETY OF CHEMISTRY

PAPER

View Article Online
View Journal | View Issue

Cite this: *Mater. Adv.*, 2022, 3, 6842

Compositional engineering of multicomponent garnet scintillators: towards an ultra-accelerated scintillation response†

Loris Martinazzoli,[ab] Saulius Nargelas,[c] Pavel Boháček,[d] Roberto Calá,[ab] Michal Dušek,[e] Jan Rohlíček,[e] Gintautas Tamulaitis,[c] Etiennette Auffray[a] and Martin Nikl*[e]

Optical, luminescence and scintillation characteristics were studied in garnet-type GAGG single-crystal scintillators grown by the Czochralski method and heavily doped with a cerium activator and a magnesium codopant at different concentrations. Emission quenching due to the formation of closely spaced Ce–Mg pairs accelerating the photoluminescence and scintillation decays down to a few nanoseconds and substantial suppression of slower decay components are observed. We show that despite a significant decrease in the scintillation yield, the coincidence time resolution and the afterglow, which are the most critically important parameters of fast scintillators, exhibited by the heavily doped GAGG:Ce,Mg are superior to those in the state-of-the-art scintillators. Due to the peculiar feature of the GAGG host to tolerate extremely high cerium and magnesium concentrations while still maintaining a bulk single crystal form, this scintillator has a great potential for high-count-rate applications in high energy physics experiments and industries with harsh operational environments, where a lower light yield can be tolerated.

Received 1st June 2022,
Accepted 11th July 2022

DOI: 10.1039/d2ma00626j

rsc.li/materials-advances

1. Introduction

Single crystal scintillators of general formula $(Gd,Lu,Y)_3(Al,Ga)_5O_{12}$:Ce, usually referred to as multicomponent garnets, were reported for the first time in combinatorial studies in 2011[1,2] and immediately gained the immense interest of the scintillator research community due to their high light yield exceeding up to three times that of classical single-crystal scintillators, such as $Y_3Al_5O_{12}$:Ce (YAG:Ce) or $Lu_3Al_5O_{12}$:Ce (LuAG:Ce) and approaching theoretical limits[3] (see ref. 4 for a review). The growth of larger single crystals enabled by the Czochralski method[5] is another practical advantage of the multicomponent garnet-type scintillators, though the necessity of using an iridium crucible due to the presence of Ga in the host composition makes their manufacturing more expensive.[6] The host with composition $Gd_3Ga_xAl_{5-x}O_{12}$ (x = 2.5–3) became the most intensively studied one, and this Ce-doped scintillator is usually referred to as GAGG:Ce in the literature. The success and origin of two- to three-fold increase in the light yield of this solid solution are based on the ability to engineer the electronic band structure of this material: the addition of Ga lowers the bottom of the conduction band immersing shallow electron traps in the lowered band edge,[7,8] whereas the Gd admixture ensures a sufficiently big energy barrier to prevent the ionization of the Ce^{3+} excited state $5d_1$.[9–11] It is, however, worth noting that GAGG:Ce scintillators cannot be used above room temperature, because the barrier becomes insufficient to prevent ionization at elevated temperatures,[12] similar to LSO:Ce.[13] Another positive contribution to the scintillation yield is caused by atomistic inhomogeneities in the cationic sublattice arrangement in GAGG, where local variations in the Ga content induce variations in the bottom of the conduction band. Such a "wavy" shape of the conduction band bottom limits the out-diffusion of electrons from the ionization track and, consequently, enhances their fast radiative recombination with holes captured at cerium ions.[14]

An essential step towards further garnet scintillator optimization was accomplished in 2014 when Mg^{2+}-codoping was shown to accelerate the scintillation decay and (for low Mg

[a] *CERN, CH-1211 Geneva 23, Switzerland*
[b] *Universitá degli Studi di Milano-Bicocca, 20126 Milano, Italy*
[c] *Institute of Photonics and Nanotechnology, Vilnius University, 10257 Vilnius, Lithuania*
[d] *Institute of Physics of the Czech Academy of Sciences, 18221 Prague, Czech Republic*
[e] *Institute of Physics of the Czech Academy of Sciences, 16200 Prague, Czech Republic. E-mail: nikl@fzu.cz*

† Electronic supplementary information (ESI) available: Compositional engineering of multicomponent garnet scintillators rev. See DOI: https://doi.org/10.1039/d2ma00626j

concentration) even to increase the light yield in the LuAG:Ce single crystal[15] and ceramics[16] following the strategy applied for Ca- and Mg-codoped LYSO:Ce.[17] Such an effect was explained by the stabilization of Ce^{4+} at the dodecahedral site of the garnet lattice. The Ce^{4+} ions can efficiently compete with electron traps for the immediate capture of electrons from the conduction band at the end of the conversion stage of the scintillation process. This provides an additional pathway for fast radiative electron–hole recombination at cerium ions and accelerates the scintillation response and reduces delayed luminescence. The combination of the band-gap and defect engineering in the multicomponent garnet family described above has been applied by many groups in the scintillation community and enabled a deeper understanding of the complex scintillation mechanisms in multicomponent garnets.[18–29]

An interesting effect of scintillation decay was revealed in 2014 in LuAG:Ce,Mg:[15] upon heavy Mg-codoping, practically all cerium ions are stabilized in the 4+ charge state: the scintillation decay is strongly accelerated and the decay time of its dominant component becomes substantially shorter (15 ns) compared to that in LuAG:Ce without codoping (58 ns). Such a decay behavior could apparently not be explained by thermal ionization of the $5d_1$ excited state of the Ce^{3+} ion. Several years later, this behavior has been explained by the formation of Ce–Mg pairs, resulting in a decreased energy barrier for luminescence quenching.[30,31]

The quest for rare events in high energy physics (HEP) requires increasing the accelerators' luminosity, *i.e.* the rate of collisions. The Large Hadron Collider (LHC) at CERN will undergo an upgrade at the end of run 3 in 2025, named the high-luminosity LHC. Precise timing will be instrumental in coping with the increased particle rate to reconstruct the particle tracks and reject background, see, for instance, the upgrade plans of CMS[32] or LHCb.[33] Co-doped GAGG:Ce,Mg crystals offer time resolutions close to that of LYSO[34] but with superior radiation hardness,[35,36] thus being strong candidates for light-based detectors in high-radiation environments. However, the relatively long decay time of the currently available GAGG crystals[34] makes them prone to suffer from a high pile-up effect of particles, thus degrading the performance of the detector. For instance, at the LHC, the proton beams are split into bunches that cross and collide every 25 ns; the decay times as long as 50–60 ns may lead to scintillation spilling over into the following bunches and signals from different particles pilling up. Consequently, accelerating the scintillation decay time without losing time resolution is of paramount importance. Moreover, if a decay time reduction were to come at the expense of light yield, it would be tolerable, because in HEP calorimetry, the energy deposited can reach up to several hundreds of GeV, and even an advantage, as some photodetectors might suffer in linearity and life expectancy. Finally, the detection of photon or particle beams has also to be accelerated down to nanosecond time scale in certain industrial applications: super high-speed X-ray imaging technologies[37] in healthcare, industrial, and research applications also need robust scintillator materials with such a fast response.

To achieve the targeted time resolution of scintillation detectors of the order of tens of picoseconds, the processes limiting the resolution have to be studied down to the picosecond and subpicosecond domains. The transient optical absorption technique in pump-probe configuration has been initially demonstrated by Prof. R. T. William's group to be a useful tool for studying CsI:Tl, NaI:Tl, SrI2:Eu[38] and later it was exploited for studying a number of scintillators including YAG, LuAG and GAGG:Ce.[39,40] This technique enables probing the population of nonequilibrium carriers in free and trapped states as well as of those at activator ions. The capability of selective excitation, simultaneous measurement of the spectrum and time evolution of transient absorption allow for the identification of components of induced absorption, whereas the time resolution of the technique is limited just by the laser pulse duration. Using a femtosecond laser enables a subpicosecond time resolution, which becomes increasingly important as the targeted time resolution of scintillator detectors approaches the low end of the picosecond domain.

In this article, we show that the structure of Czochralski-grown GAGG:Ce,Mg bulk single crystals allows for high concentrations of the Ce dopant and the Mg codopant, wherein the scintillation decay can be accelerated down to units-of-nanoseconds time scale, which is by a factor of ten faster compared to those reported on Czochralski-grown multicomponent garnets in earlier publications.[34,41] Though such a scintillation acceleration is achieved at the expense of light yield, other scintillation characteristics remain competitive. Thus, this material can find applications in high energy physics and industry where such a fast response is critical and a lower light yield can be tolerated.

2. Experimental section

2.1. Crystal growth and analysis

A GAGG:Ce,Mg single-crystal boule with a diameter of about 12.5 mm (see Fig. 1) was grown at the Institute of Physics of the Czech Academy of Sciences using the Czochralski method from the melt in the iridium crucible under an atmosphere of nitrogen with the addition of 2% oxygen by using the *Cyberstar Mini-oxypuller* machine. The initial melt content corresponded to the composition $Gd_{2.955}Ce_{0.015}Mg_{0.03}Ga_3Al_2O_{12}$. Consuming nearly all the melt in the growth process with segregation

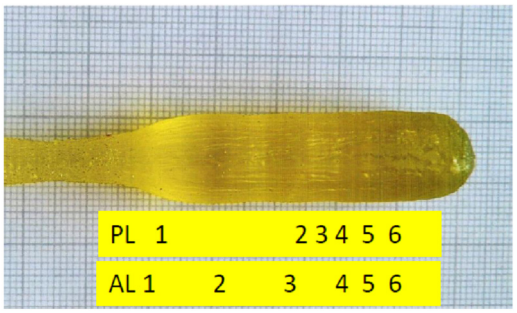

Fig. 1 Photograph of the GAGG:Ce,Mg crystal grown using the Czochralski method. Positions of plates used for characterization experiments (PL1–6) and compositional analysis (AL1–6) are indicated.

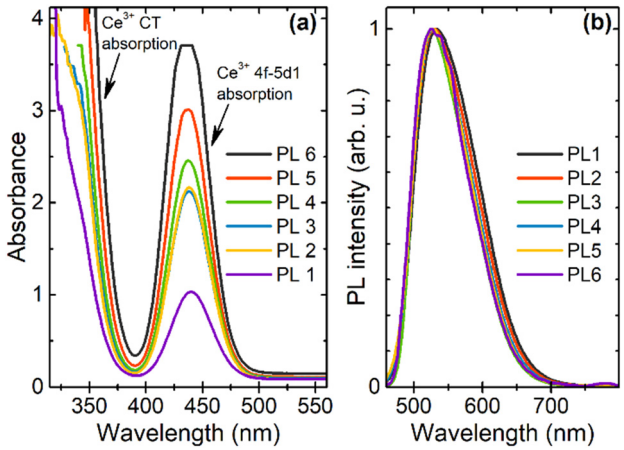

Fig. 2 Absorption (a) and normalized photoluminescence (b) spectra of six GAGG:Ce,Mg plates PL1–6.

coefficients of Ce and Mg in the GAGG host lower than 1, the content of the Ce dopant and Mg codopant along the boule growth axis increases (see absorption spectra in Fig. 2). A set of plates, PL1 to PL6, was prepared by cutting from the boule at the positions indicated in Fig. 1. The plates were used in optical, luminescence and scintillation measurements. Another set of plates, AL1 to AL6, was prepared for composition analysis. Plates AL4,5,6 were the same as PL4,5,6. All the plates were 1.2 mm thick with both faces polished. Starting from PL3, towards the crystal end, tiny, hardly visible inclusions appear in the crystal volume.

The chemical analysis of AL1–6 plates, as shown in Table 1, was made using the electron microanalyzer Jeol JX-8230 with energy – dispersive spectrometer Bruker QUANTAX 200 and using software Esprit 2.2. X-Ray diffraction (XRD) analysis of a sample cut just behind the AL6 plate confirmed the cubic garnet structure fairly matching the 04-023-5738 card in the database PDF4+, corresponding to composition $Gd_{2.985}Ce_{0.015}Ga_3Al_2O_{12}$ without the presence of any parasitic phases. The detailed Rietveld fitting in the crystallographic computing system Jana2020 revealed two garnet phases with very close elementary cell parameters, a_1 = 12.28279(5) Å and a_2 = 12.29436(13) Å, with their volume ratio of 0.8 : 0.2. The details of this analysis are presented in Fig. S1 of the ESI;† the origin of this structural peculiarity is not clear yet.

Table 1 Composition of plates AL1-6. "SC" stands for starting composition of the melt, the content values correspond to the coefficients in the chemical formula (*e.g.*, $Gd_{2.955}Ce_{0.015}Mg_{0.03}Ga_3Al_2O_{12}$ for SC), and "*g*" is the fraction of melt volume consumed in the growth process at the position of the plate

	g	Gd	Ce	Mg	Ga	Al
SC		2.955	0.015	0.03	3	2
AL1	0.065	2.917	0.0065	0.0051	2.787	2.284
AL2	0.155	2.944	0.0063	0.0053	2.813	2.231
AL3	0.416	2.978	0.0096	0.0058	2.845	2.160
AL4	0.618	2.954	0.0131	0.0039	3.043	1.986
AL5	0.703	2.959	0.0164	0.0060	3.108	1.982
AL6	0.789	2.952	0.0279	0.0112	3.251	1.758

The composition analysis shows that growing just a single boule consuming nearly all the volume of the melt in the crucible and cutting samples along the boule axis enabled us to fabricate a set of GAGG:Ce,Mg samples with the content of Ce increasing in samples from PL1 to PL6 in a wide range up to heavy doping corresponding to the substitution of ~1% of cations by the sum of Ce and Mg.

2.2. Methods and instrumentation

At the Institute of Physics of the Czech Academy of Sciences, the radioluminescence spectra and the photoluminescence decay upon excitation by the X-ray tube (*Seifert GmbH*) operated at 40 kV and pulsed nanoLED 450 nm (*Horiba IBH Scotland*), respectively, were recorded using a custom-made spectrofluorimeter based on 5000M *Horiba Jobin Yvon* equipped with TBX-04 photon counting. Time-correlated single photon counting (1.2 ns FWHM of the measured instrumental response) was used in the luminescence decay measurements, whereas the decay was deconvoluted from the instrumental response using SpectraSolve software package *Amex Photonics*. The absorption spectra were recorded using the *Shimadzu 3101 PC* spectrometer.

Experiments at CERN were performed using 1 × 1 × 5 mm^3 samples cut out from each plate. Two opposite side faces were optically polished, and all other faces were ground. For reference, three samples of the same size were prepared from commercial GAGG:Ce fibers purchased from three producers: C&A (Japan), Institut Lumière Matière (ILM, France), and Fomos (Russia). These reference samples had only one-end face ground and the remaining ones were optically polished. Thus, the light output of the two sample groups was slightly influenced by the different surface conditions. Nevertheless, the reference samples provide a valuable indication of the current state of the art of commercial GAGG scintillators.

The light output was measured at 20 °C after wrapping the samples in a Teflon tape and coupling their 1 × 1 mm^2 face to the calibrated *Hamamatsu* photomultiplier tube (PMT) R2059. The PMT current was integrated within a 500 ns gate. A ^{137}Cs source was used for excitation.

The coincidence time resolution (CTR) is defined as the resolution of the difference in detection time of two 511 keV back-to-back gamma photons produced by a ^{22}Na source. The samples were wrapped in a Teflon tape and coupled to silicon photomultipliers (SiPMs) HPK S13360-3050PE. The set-up is described in ref. 42 and more details on the measurements are provided in ref. 34.

The scintillation kinetics of the samples was measured employing two time-correlated single photon counting (TCSPC) set-ups. The first set-up had a picosecond-pulse X-ray tube (<40 keV) as an excitation source and the stop detector realized by Hybrid Photomultiplier tube HPM 100-07 *Becker & Hickl* (see ref. 43 for more details). A bandpass filter with a 40 nm FWHM band centered at 550 nm was employed to reduce stray light. The second set-up exploited excitation by 511 keV gamma photons emitted by a ^{22}Na source. The set-up is described in ref. 44.

The scintillation kinetics was described by a multi-exponential function with one rise time τ_r and three decay times $\tau_{d,i}$ as in ref. 43:

$$f(\theta) = \Theta(t-\theta)\sum_{i=1}^{3} A_i \cdot \frac{e^{-t/\tau_{d,i}} - e^{-t/\tau_r}}{\tau_{d,i} - \tau_r} \quad (1)$$

This was convolved with the instrumental response function (IRF) of the set-up and fitted to the data. The effective decay time was defined as:

$$\frac{1}{\tau_{d,\mathrm{eff}}} = \sum_{i=1}^{3} \frac{A_i}{\tau_{d,i}} \quad (2)$$

measurements of the temperature dependence of photoluminescence decays and room temperature transient absorption were performed at the Institute of Photonics and Nanotechnology, Vilnius University. The photoluminescence decay kinetics in the subnanosecond domain was measured using a Yb:KGW laser (Pharos, Light Conversion), delivering 250 fs pulses at 1030 nm as an excitation source. The photon energy has been tunably adjusted using an optical parametric amplifier (*Orpheus*, *Light Conversion*) and stepwise increased in a harmonic generator to resonantly excite Ce^{3+} activator ions. The *Becker&Hickl* TCSPC module SPC-130 coupled with a cooled photomultiplier (PMC-150) was exploited to record the photoluminescence decay with a time resolution of 200 ps. The dynamics of nonequilibrium carriers was studied in a pump and probe configuration using the transient absorption (TA) technique. The output of the femtosecond Yb:KGW laser was divided into pump and probe beams. The pump beam was equipped with an optical parametric amplifier and a harmonic generator to tune the pump photon energy for resonant excitation of Ce^{3+} activator ions to their excited levels $5d_1$ and $5d_2$. The TA amplitude is proportional to the population of the photoexcited electrons and was probed by the second beam converted to a white light supercontinuum in the range from 1.3 to 2.7 eV (950–460 nm) after sharp focusing in a sapphire plate. The probe beam was equipped with an optomechanical delay stage enabling a tuneable delay from 0 to 10 ns between pump and probe pulses with a subpicosecond precision. Thus, the setup enabled measuring the time evolution of the TA spectrum with a subpicosecond time resolution (see [ref. 45] for more details).

3. Results and discussion

3.1. Absorption and photoluminescence spectra and decays

The absorption spectra presented in Fig. 2(a) evidence a progressive increase of Ce^{4+} and Ce^{3+} as reflected by enhanced characteristic charge transfer (CT) absorption of Ce^{4+} below approx. 380 nm and the 4f–$5d_1$ absorption band of Ce^{3+} peaking at 440 nm, respectively. This is consistent with the increasing Ce content in PL1 → PL6 samples (Table 1). It is the consequence of the cerium segregation coefficient being lower than one (estimated from the values of the Ce content in SC and AL1 in Table 1 to be about 0.4) and the consumption of nearly all the crucible content in the growth process.

PL spectra under excitation *via* the 4f-$5d_1$ absorption transition of Ce^{3+}, as shown in Fig. 2(b), show a typical broad $5d_1$-4f Ce^{3+} emission band. The absorption and emission bands show a systematic blue shift along the crystal growth axis, in consistence with the increase of Ga concentration (see Table 1), which is known to cause a blue shift of the Ce^{3+} 4f-$5d_1$ absorption and emission transitions.[1]

The photoluminescence decays measured at the excitation and emission wavelengths of 452 nm and 530 nm, respectively, are presented in Fig. 3. The decay in sample PL1 with the lowest content of Ce and Mg is nearly single-exponential with a decay time of 46 ns. The decay in sample PC1, which has been prepared with similar Ce content as in PL1, but without Mg codoping, is also nearly single-exponential with a decay time of 55.1 ns. In plate PL4 with a much higher content of Ce and Mg, the decay becomes substantially accelerated and non-exponential with its dominant fast component having a decay time of about 15 ns. However, sample PC 4, a Mg-free analog of PL4, exhibits a nearly single-exponential decay with the decay time of 48.3 ns of the dominant component, *i.e.* the decays of PC1 and PC4 are quite similar. Thus, the presence of Mg is proved to be essential for the photoluminescence decay acceleration in GAGG:Ce, in consistent with the conclusions in ref. 30 and 31. The decays of all the samples PL1–PL6 approximated by a sum of two exponentials are shown for mutual comparison in Fig. S2 in the ESI.†

3.2. Temperature dependence of photoluminescence intensity and decay

Temperature dependence of the time- and spectrally-integrated photoluminescence intensity is presented in Fig. 4 for two

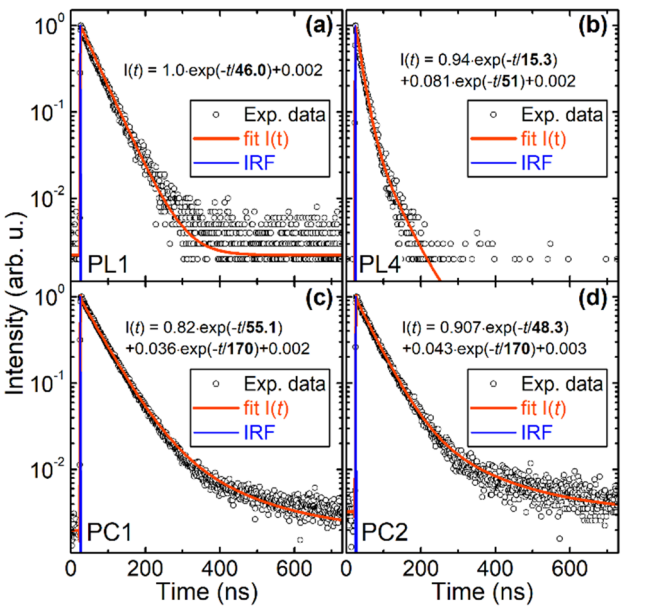

Fig. 3 Normalized photoluminescence decays in GAGG:Ce,Mg samples PL1 and PL4 and the reference Mg-free samples PC1 and PC4 with similar Ce content and host composition: $Gd_{2.980}Ce_{0.0053}Ga_{2.520}Al_{2.361}O_{12}$ for PC1 and $Gd_{3.002}Ce_{0.0138}Ga_{2.825}Al_{1.983}O_{12}$ for PC4. Solid lines are convolutions of mono- or bi-exponential functions *I*(*t*) and instrumental response IRF.

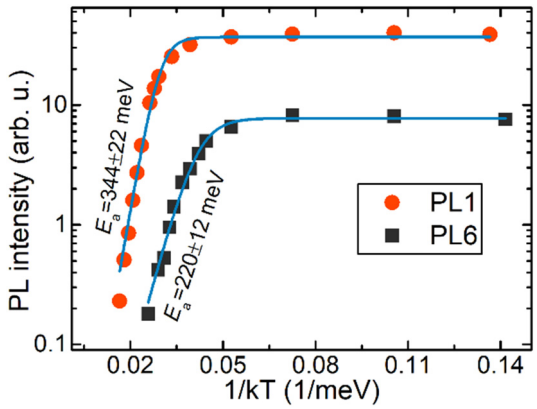

Fig. 4 Temperature dependence of time- and spectrally-integrated photoluminescence intensity of plates PL1 and PL6 under 442 nm excitation by 250 fs laser pulses.

samples containing the lowest (PL1) and highest (PL6) Ce content. It can be properly described by a single activation energy E_a according to the formula

$$V(t) = \frac{V_{lowT}}{1 + A \cdot \exp\left(-\frac{E_a}{kT}\right)}, \quad (3)$$

where V_{lowT} is the constant PL intensity value at low temperatures and A is a fitting constant. The activation energy E_a for emission quenching decreases with the increasing Ce content from 344 meV in PL1 down to 220 meV in PL6.

For plate PL1, the photoluminescence decay curves at different temperatures in the range from 85 K to 700 K are presented in the ESI,† Fig. S3(a). The decay curves at elevated temperatures are close to a single exponential decay, whereas a bi-exponential decay is observed below ~160 K. The decay times were extracted by the exponential fitting of decay curves (see Fig. 5a)) and the component of the highest intensity (circled points in Fig. 5) was found after the calculation of partial intensities of each decay component as $A_i\tau_i/\sum A_i\tau_i$. The temperature dependence of the decay time of the highest-intensity component is well described by eqn (1) with the values for the decay time as V and with an activation energy E_a of 362 ± 11 meV, which is close to that derived from the temperature dependence of the spectrally integrated photoluminescence intensity as shown in Fig. 4.

A quite different situation is observed in heavily doped sample PL6 (see Fig. S3(b) in the ESI†): the decay can be properly fitted only by involving three decay components, fast, medium and slow, with the low-temperature decay time constants of 1.2, 7, and 37 ns, respectively. Thermal quenching of these components can be separately described by eqn (1) with decreasing activation energies E_a of 323 ± 30, 236 ± 13, and 145 ± 5 meV for fast, medium, and slow components, respectively (see Fig. 5(b)). Only the activation energy of the medium component is close to that obtained for photoluminescence intensity quenching as shown in Fig. 4.

The strongly nonexponential and substantially faster luminescence decay in PL6 at low temperatures even at resonant

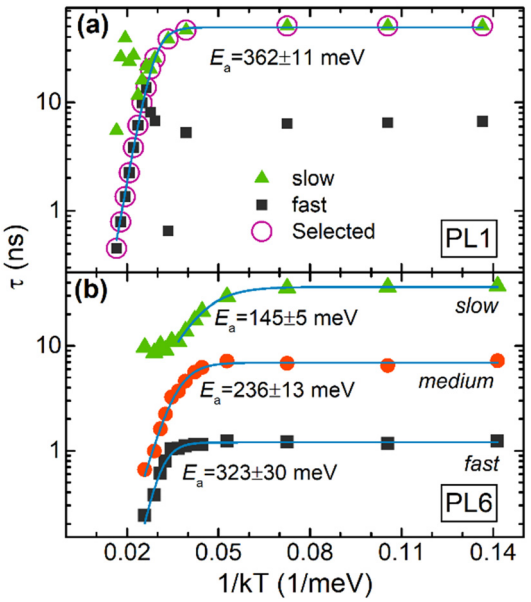

Fig. 5 Temperature dependence of photoluminescence decay times in sample PL1 (a) obtained from single- and bi-exponential fits of the decays and in sample PL6 (b) obtained from three-exponential fits of the decay curves, as described in the text. Solid lines represent approximations using eqn (1), and activation energies are indicated.

excitation to the $5d_1$ emitting level of Ce^{3+} evidences the presence of significant channels of nonradiative recombination for the electrons which have relaxed here. The obtained experimental results conclusively lead to the assumption that the nonradiative channels are caused by Ce–Mg pairs. The existence of at least three different activation energies for luminescence quenching might be interpreted by the contribution of Ce^{3+} ions paired with Mg ions at different distances (see Section 3.8 below), which are unavoidably discrete due to the available positions of Mg in the crystal structure.

3.3. Transient absorption measurements

The first stages of the population of emitting level $5d_1$ of the activator ion Ce^{3+} have been studied using the transient absorption (TA) technique. Resonant excitations directly to the levels $5d_1$ and $5d_2$ have been exploited. At resonant excitation to $5d_1$, the TA spectrum was centered at 1.4 eV and the rising part of the TA response was instantaneous within the time resolution of ~250 fs. These features are expected for TA probing the population of resonantly excited level $5d_1$, as mentioned in ref. 40 and 46. After the resonant excitation to the $5d_2$ level, which is already in the conduction band of the matrix crystal GAGG,[9,12] the nonequilibrium electrons have two routes to relax to the level $5d_1$: intracenter relaxation with the time constant of ~500 fs, as mentioned in ref. 40 and *via* the extended states in the conduction band. The importance of the latter route is evidenced by the presence of another TA component spectrally centered at 1.7 eV. The rise time of the TA response due to the population of $5d_1$ after electron relaxation *via* the conduction band is usually attributed to the time

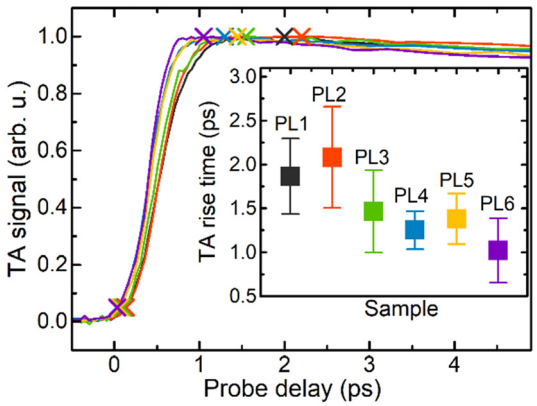

Fig. 6 Initial part of the transient absorption response to a short-pulse (250 fs) excitation of six samples with the increasing doping level in the samples from PL1 to PL6. The inset shows the rise times (see the text for their definition) for the samples.

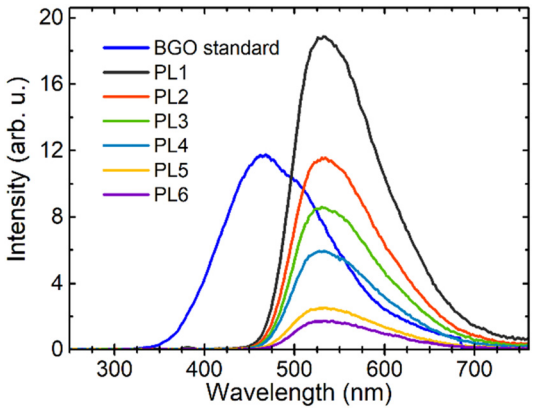

Fig. 8 Radioluminescence spectra of GAGG:Ce,Mg samples PL1–PL6 and a standard BGO sample under X-ray excitation (40 kV).

necessary for the electrons relaxed to the bottom of the conduction band or possibly to certain shallow traps to get back to the cerium ion, as mentioned in ref. 40. This part of the TA response is presented in Fig. 6. The inset in Fig. 6 shows the rise time defined as the time period between the moment corresponding to the peak TA and the moment corresponding to 5% of the peak value (indicated by crosses in the main figure) for all samples studied. The rise time decreases with the increasing doping level from plate PL1 towards PL6 and is shorter than those observed in GAGG:Ce before.[40]

The TA decay within the first few nanoseconds is presented in Fig. 7. The data carpets for excitation to $5d_1$ and $5d_2$ levels are shown in Fig. 7(a) and (b), respectively, whereas the decay kinetics at typical probe photon energies are presented in Fig. 7 (c).

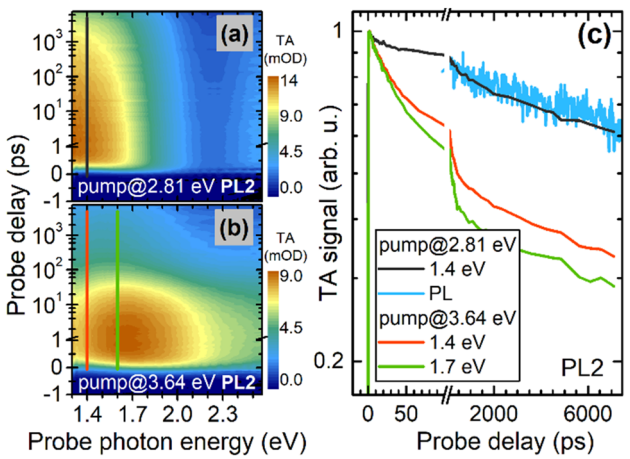

Fig. 7 Data carpets for the transient absorption as a function of the probe photon energy and the delay between pump and probe pulses under excitation of Ce^{3+} ions to their lowest excited level $5d_1$ (a) and the second lowest level $5d_2$ (b) and the transient absorption decay kinetics (c) for pump and probe photon energies as indicated in the legend in (c) and marked by vertical lines of the corresponding color in (a and b). For comparison, the decay of resonantly excited ptotoluminescence is presented in blue.

The decay is strongly nonexponential. It is worth noting that a nonexponential decay is also observed at probing the population of the lowest excited state $5d_1$ after resonant excitation to this level. This is an indication that the electrons disappear from the level $5d_1$ by radiative recombination which should result in an exponential decay of the population. After excitation to $5d_2$, the initial part of the TA decay is also affected by the electrons relaxing *via* the conduction band, whereas the decay after the first few nanoseconds proceeds at the same rate as that at excitation to $5d_1$.

3.4. Radioluminescence spectra

Radioluminescence spectra (see Fig. 8) are dominated by the Ce^{3+} emission band having a shape similar to that observed in photoluminescence (Fig. 2). The radioluminescence intensities of samples PL1–PL6 and standard BGO are quantitatively compared in Fig. 8. The observed gradual decrease of luminescence intensity in the sequence of samples from PL1 to PL6 is consistent with the acceleration of the photoluminescence decay (see Fig. S2 in the ESI†).

3.5. Light output

Light output was calculated using the photopeak position under ^{137}Cs excitation in all samples except for the sample PL6 due to its low light output, which produced a total charge during scintillation events comparable to background events and an unresolved photopeak. However, the background events featured a time-profile different from the scintillation events, hence a different pulse amplitude for the same integrated charge is achieved, which separates the two groups. Rejecting the background with this pulse-shape discrimination made possible extracting the average light output for scintillation events and comparing it to that in other samples.

The light output in the tested GAGG samples ranged from 500 to 12 000 photons per MeV (see Table 2) and was lower than that in the commercial reference samples. We also note that light output achieved at reference samples was lower than that reported for the same material in the literature[34] due to the higher aspect-ratio of the sample geometry employed here.

Table 2 GAGG:Ce,Mg light output measured in samples PL1 to PL6 and commercial samples for reference

Sample	Light output (ph MeV^{-1})	Commercial sample	Light output (ph MeV^{-1})
PL1	12 000 ± 600	GFAG C&A	20 500 ± 1000
PL2	7600 ± 380	GAGG Fomos	28 300 ± 1400
PL3	5200 ± 260	GAGG ILM	21 000 ± 1100
PL4	3900 ± 190		
PL5	2300 ± 230		
PL6	500 ± 300		

3.5. Scintillation decay

The scintillation decays for all samples PL1–PL6 measured under picosecond pulse X-ray and ^{22}Na radioisotope 511 keV excitation are presented in Fig. 9 and Fig. S4, S5 in the ESI,† respectively. The parameters of the rise and decay components extracted from experimental results obtained at X-ray and gamma-ray excitation are summarized in Table 3 and Table S1 in the ESI,† respectively. The scintillation decay is accelerated with the increasing doping level consistently with the photoluminescence decay (Fig. S2 in the ESI†). All the samples exhibit scintillation decay considerably faster than that in the reference samples, and no slow component is resolved above 80 ns. The calculated rise time is below the instrumental time resolution for all the samples excited by X-rays.

In Fig. 10, the decays of photoluminescence and radioluminescence (excitation with X-rays and 511 keV photons of radioisotope ^{22}Na) are compared for samples PL1 and PL6 (the decays for samples PL2 to PL5 are presented in Fig. S6 in the ESI†). Scintillation decays under X-ray and gamma-ray excitation are significantly accelerated compared to the photoluminescence ones, which deserves a comment: it is known that if a high density of elementary excitations occurs locally, they might start to interact, which results in an efficiency loss reflected, *e.g.*, in the light yield loss[47] and accelerated luminescence decay.[48] Such locally high excitation density occurs along the ionization track when the excitation by X-ray or gamma-ray photons is used.[49] The local density even increases with the decreasing energy of excitation photons (*i.e.*, it is higher upon X-ray excitation in this case), which explains the observed differences in the course of the decay curves as shown in Fig. 10 and Fig. S6 (ESI†).

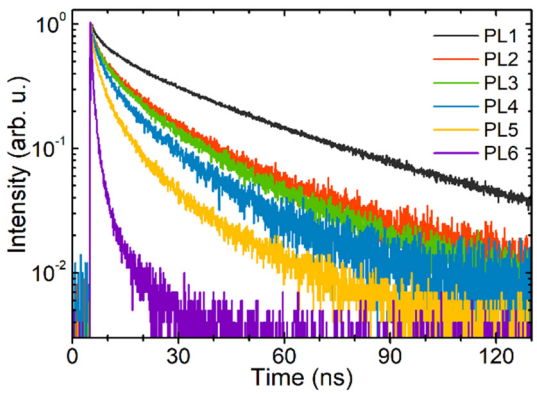

Fig. 9 Scintillation decay in samples PL1–PL6 under excitation by picosecond X-ray pulses.

Table 3 Scintillation rise time (τ_r), three decay times (τ_{d1}, τ_{d2}, τ_{d3}), and relative intensities of the corresponding components R_1, R_2, R_3 after X-ray excitation. The uncertainty is 25 ps and 5%, for the rise and decay times, respectively. $\tau_{d,eff}$ is defined by eqn (2)

Sample	τ_r (ps)	τ_{d1} (ns)	R_1 (%)	τ_{d2} (ns)	R_2%	τ_{d3} (ns)	R_3 (%)	$\tau_{d,eff}$ (ns)
C&A GFAG	32	6.0	4.6	44.5	69.2	222	26.3	41
ILM GAGG	37	4.0	3.2	40.4	56.4	138	40.4	40
Fomos GAGG	30	2.2	0.5	53.1	41.7	166	57.8	73
PL1	13	2.5	3.3	25.4	48.0	79.2	48.8	26
PL2	8	2.1	7.2	16.6	54.6	66.2	38.2	13.8
PL3	5	1.6	6.2	12.6	47.5	46.0	46.3	11.6
PL4	5	1.5	9.2	11.3	53.9	45.4	36.9	8.6
PL5	5	1.0	11.0	7.1	51.8	40.8	37.2	5.2
PL6	5	0.2	19.5	1.5	53.0	14.9	27.5	0.7

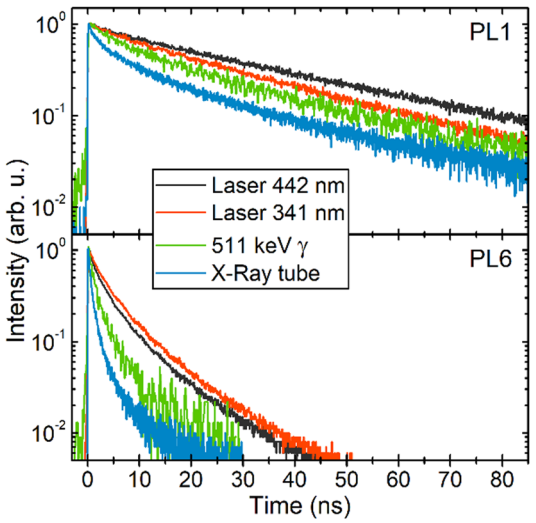

Fig. 10 Luminescence decay after excitation by the 341 and 442 nm laser pulses, picosecond X-ray pulses, and 511 keV photons in samples PL1 and PL6.

3.6. Coincidence time resolution

The CTR values measured for 1 × 1 × 5 mm^3 samples are presented in Table 4. The samples under study have similar CTRs except for sample PL6 having very low light output at 511 keV excitation and large uncertainty in the CTR estimation.

It is worth noting that the CTR of the samples studied is comparable with that in the commercial reference samples. Thus, all the samples exhibit competitive timing performance in spite of the strong reduction in their light output.

The scintillator time resolution characterized as CTR is known to be proportional to the square root of the decay time ($\tau_{d,eff}$) to the light output (LO) ratio[42,50,51] According to our results on the time evolution of the population of the emitting level of the activator ion Ce^{3+}, the rise time (τ_r) in the studied samples can be assumed to be equal within the experimental uncertainty. Thus, the fact that the various samples show

Table 4 Coincidence time resolution (CTR) measured for $1 \times 1 \times 5$ mm^3 samples wrapped in a Teflon tape and coupled using optical grease Rhodorsil to SiPM HPK13360 3050PE

Sample	CTR (ps)	Commercial sample	CTR (ps)
PL1	143 ± 3	GFAG C&A	127 ± 3
PL2	149 ± 3	GAGG Fomos	154 ± 3
PL3	141 ± 3	GAGG ILM	133 ± 3[a]
PL4	136 ± 5		
PL5	148 ± 5		
PL6	170 ± 10		

[a] No well-defined photopeak.

similar CTR with different doping content demonstrates how the doping-induced reduction in the light yield is compensated by the decrease of the decay time. As a result, a significant shortening of the scintillation decay time is achieved by heavy doping of GAGG:Ce,Mg at no significant degradation of the time resolution in CTR experiments.

3.7. Afterglow

The afterglow of all the samples was studied up to 250 ms. The results are shown in Fig. 11 in comparison with the afterglow in a standard BGO sample. Scintillation intensity drop by nearly four orders of magnitude is observed in all the samples within 10–15 ms after X-ray excitation is terminated. The drop is comparable with that in BGO which is known as an extremely low-afterglow scintillation material.

3.8. Ce–Mg pairs: model considerations

The correlation of the increase in the Ce + Mg concentration with the simultaneous decrease in the scintillation intensity and the light yield accompanied by the acceleration of photoluminescence and scintillation decays described above is a clear indication that the Ce–Mg pairs introduce an additional channel for emission quenching. It is interesting to find out the average distance at which the Ce and Mg ions can build a pair. The distance might be estimated just from the Ce–Ce distance and its dependence on Ce concentration. In Fig. 12, the number

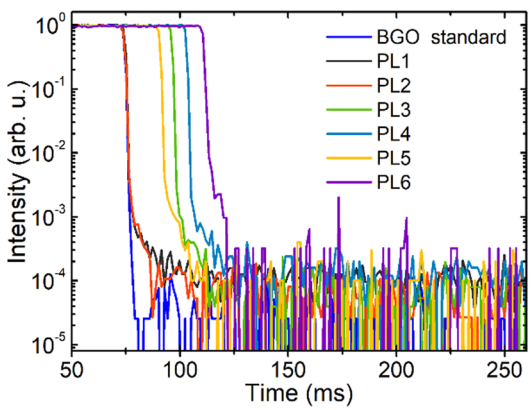

Fig. 11 Spectrally integrated afterglow in samples PL1–PL6 and standard BGO sample for reference after X-ray excitation (40 kV 15 mA^{-1}). The curves are shifted horizontally for clarity.

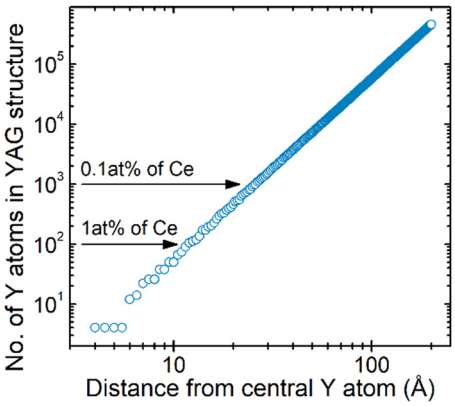

Fig. 12 Calculated number of yttrium cations contained within a sphere in the YAG lattice around a single Y cation as a function of the sphere diameter. Arrows indicate the average Ce–Ce distance at the indicated Ce concentrations in the crystal.

of yttrium cations in the analogous YAG structure is calculated as a function of the diameter of the sphere around a central yttrium ion. For the cerium concentration at the level of 1 at% (1 cerium ion per 100 yttrium ions), the average Ce–Ce distance is about 12 Å, which means that Mg ions added at similar or even lower concentrations can constitute Ce–Mg pairs with an average distance of about 6 Å. For 0.1 at% Ce, this estimated Ce–Mg average distance is equal to 13 Å. In the former case, there are only about 10 dodecahedral sites available, so that the set of available Ce–Mg distances will have a distinct discrete character. In sample PL6, Ce concentration is so high that the photoluminescence decay at low enough temperatures can be approximated by a sum of three exponentials (see Section 3.2 and Fig. S3 in the ESI†), which could be interpreted by the dominating emission of the Ce–Mg pairs separated at three available distances resulting in three dominating quenching processes governed by different energy barriers.

4. Conclusions

The cubic structure of GAGG allows embedding a very high concentration of cerium dopant and magnesium codopant, up to approx. 1 at% and 0.5 at%, respectively, in the Czochralski-grown single crystal without deteriorating the high structural quality of the single crystal evidenced by XRD measurements. Such a heavily doped crystal does tend to contain micrometer-sized inclusions of parasitic phases with their density increasing towards the crystal end. Thus, further growth procedure optimization is necessary to eliminate such inhomogeneities.

At the highest achieved Ce and Mg concentrations, the average distance between the ions in Ce–Mg pairs becomes smaller than 10 Å. As a result, just a few discrete structure-determined distances are available for the partners in the pair. Upon acceptance of the hypothesis of emission quenching in Ce–Mg pairs provided in recent papers,[30,31] such a situation can explain the observation of two- or three-exponential decay in a wide temperature range up to a certain limit above which the

classical thermal quenching overrides the effect of quenching in Ce–Mg pairs.

Transient absorption measurements show that the population of the Ce^{3+} emitting level $5d_1$ after excitation to the $5d_2$ level (situated in the conduction band) becomes larger with the increasing doping level. This effect might be interpreted by Coulomb-interaction-enhanced acceleration of electron capture by Ce^{4+}, germinal or external, with increasing Ce-doping.

Scintillation efficiency and light yield smoothly decrease with the increasing Ce and Mg content, whereas both the scintillation and photoluminescence decays are accelerated. The dominant decay components in photoluminescence and scintillation show similar values of the characteristic decay times, well below 10 ns at the highest dopant concentration, which proves the absence of any decelerating processes in the scintillation mechanism. Despite the significantly lowered light yield in the crystal with increasing doping, the CTR values remain competitive with those of the fastest GAGG-based scintillators reported in the literature so far. Moreover, the samples feature an ultralow afterglow on the millisecond time scale. Such a combination of scintillation characteristics makes this material very competitive for precision timing in high-luminosity HEP experiments and high-speed X- and gamma-ray imaging and beam diagnostics in industry and medical applications. For instance, the accelerated decay time will be instrumental to mitigate the pile-up of signal spilling over from one bunch crossing to the next ones in detectors at the high-luminosity LHC, or any future collider, without loss of time resolution, crucial for reconstructing the multiple tracks produced in the particle collisions.

The results of this study expand significantly the range of applications that GAGG:Ce,Mg can cover, as this scintillator is proved to be a versatile material with scintillation properties that can be finely tuned by varying the material composition according to the application requirements.

Author contributions

M. N. provided the idea, planned experiments and supervised all the project. P. B. grew the crystals. L. M., R. C., S. N., and J. R. performed the experiments and evaluated the data. M. D. calculated the distribution of yttrium atoms in the YAG structure. E. A. and G. T. and M. N. supervised experiments at CERN, Vilnius and Prague labs, respectively. M. N., G. T., L. M., R. C., and E. A. wrote the manuscript. All the authors discussed the results and commented on the paper.

Conflicts of interest

There are no conflicts to declare.

Acknowledgements

This work was carried out in the framework of Crystal Clear Collaboration. It was partially supported by the HORIZON 2020 RIA project AIDAinnova under Grant Agreement No. 101004761. The support of Czech Science Foundation project no. 21-17731S and of Operational Programme Research, Development and Education financed by European Structural and Investment Funds and the Czech Ministry of Education, Youth and Sports (Project No. SOLID21 CZ.02.1.01/0.0/0.0/16_019/0000760) is gratefully acknowledged. We are thankful to J. Ryšavý for the help with the crystal growth procedures, A. Beitlerova and R. Kucerkova for performing the absorption and radioluminescence spectra and photoluminescence decays measurements, to A. Vaitkevičius for spatially resolved photoluminescence measurements, to K. Jurek for the electron microprobe analysis of the samples, and to D. Deyrail for the preparation of the $1 \times 1 \times 5$ mm^3 samples.

References

1 K. Kamada, T. Yanagida, T. Endo, K. Tsutumi, Y. Fujimoto, A. Fukabori, A. Yoshikawa, J. Pejchal and M. Nikl, Composition engineering in Ce doped $(Lu,Gd)_3(Ga,Al)_5O_{12}$ single crystal scintillators, *Cryst. Growth Des.*, 2011, **11**, 4484–4490.

2 K. Kamada, T. Yanagida, J. Pejchal, M. Nikl, T. Endo, K. Tsutumi, Y. Fujimoto, A. Fukabori and A. Yoshikawa, Scintillator-oriented combinatorial search in the Ce doped $(Y,Gd)_3(Ga,Al)_5O_{12}$ multicomponent garnet compounds, *J. Phys. D: Appl. Phys.*, 2011, **44**, 505104.

3 P. Dorenbos, Fundamental limitations in the performance of Ce^{3+}, Pr^{3+}, and Eu^{2+} activated scintillators, *IEEE Trans. Nucl. Sci.*, 2010, **57**, 1162–1167.

4 M. Nikl, A. Yoshikawa, K. Kamada, K. Nejezchleb, C. R. Stanek, J. A. Mares and K. Blazek, Development of LuAG-based Scintillator Crystals – A Review, *Prog. Cryst. Growth Charact. Mater.*, 2013, **59**, 47–72.

5 K. Kamada, T. Yanagida, T. Endo, K. Tsutumi, Y. Usuki, M. Nikl, Y. Fujimoto, A. Fukabori and A. Yoshikawa, 2 inch diameter single crystal growth and scintillation properties of Ce:$Gd_3Al_2Ga_3O_{12}$, *J. Cryst. Growth*, 2012, **352**, 88–90.

6 O. Sidletskiy, *et al.*, Garnet Crystal Growth in Non-precious Metal Crucibles, Proceedings of ISMART 2018, in *Engineering of Scintillation Materials and Radiation Technologies*, ed. M. Korzhik and A. Gektin, Springer Proceedings in Physics, Springer, Cham, 2019, vol. 227, pp. 83–95.

7 M. Nikl, J. Pejchal, E. Mihokova, J. A. Mares, H. Ogino, A. Yoshikawa, T. Fukuda, A. Vedda and C. D'Ambrosio, Antisite defect-free $Lu_3(Ga_xAl_{1-x})_5O_{12}$:Pr scintillator, *Appl. Phys. Lett.*, 2006, **88**, 141916.

8 M. Fasoli, A. Vedda, M. Nikl, C. Jiang, B. P. Uberuaga, D. A. Andersson, K. J. McClellan and C. R. Stanek, Band-gap engineering for removing shallow traps in rare-earth $Lu_3Al_5O_{12}$ garnet scintillators using Ga^{3+} doping, *Phys. Rev. B: Condens. Matter Mater. Phys.*, 2011, **84**, 081102.

9 P. Dorenbos, Electronic structure and optical properties of the lanthanide activated $RE_3(Al_{1-x}Ga_x)_5O_{12}$ (RE = Gd, Y, Lu) garnet compounds, *J. Lumin.*, 2013, **134**, 310–318.

10 I. I. Vrubel, R. G. Polozkov, I. A. Shelykh, V. M. Khanin, P. A. Rodnyi and C. R. Ronda, Bandgap Engineering in

Yttrium–Aluminum Garnet with Ga Doping, *Cryst. Growth Des.*, 2017, **17**, 1863–1869.

11 J. Ueda, A. Meijerink, P. Dorenbos, A. J. Bos and S. Tanabe, Thermal ionization and thermally activated crossover quenching processes for 5d-4f luminescence in $Y_3Al_{5-x}Ga_xO_{12}$: Pr^{3+}, *Phys. Rev. B*, 2017, **95**, 014303.

12 J. M. Ogiegło, A. Katelnikovas, A. Zych, T. Justel, A. Meijerink and C. R. Ronda, Luminescence and Luminescence Quenching in $Gd_3(Ga,Al)_5O_{12}$ Scintillators Doped with Ce^{3+}, *J. Phys. Chem. A*, 2013, **117**, 2479–2484.

13 E. van der Kolk, S. A. Basun, G. F. Imbusch and W. M. Yen, Temperature dependent spectroscopic studies of the electron delocalization dynamics of excited Ce ions in the wide band gap insulator, Lu_2SiO_5, *Appl. Phys. Lett.*, 2003, **83**, 1740–1742.

14 A. Belsky, A. Gektin and A. N. Vasil'ev, Influence of Disorder in Scintillating Solid Solutions on Thermalization and Recombination of Electronic Excitations, *Phys. Status Solidi B*, 2020, **257**, 1900535.

15 M. Nikl, K. Kamada, V. Babin, J. Pejchal, K. Pilarova, E. Mihokova, A. Beitlerova, K. Bartosiewicz, S. Kurosawa and A. Yoshikawa, Defect-engineering in Ce-doped aluminum garnet single crystal scintillators, *Cryst. Growth Des.*, 2014, **14**, 4827–4833.

16 S. Liu, X. Feng, Z. Zhou, M. Nikl, Y. Shi and Y. Pan, Effect of Mg^{2+}Co-Doping on the Scintillation Performance of LuAG:Ce ceramics, *Phys. Status Solidi RRL*, 2014, **8**, 105–109.

17 S. Blahuta, A. Bessiere, B. Viana, P. Dorenbos and V. Ouspenski, Evidence and consequences of Ce^{4+} in LYSO:Ce, Ca and LYSO:Ce,Mg single crystals for medical imaging applications, *IEEE Trans. Nucl. Sci.*, 2013, **60**, 3134–3141.

18 W. Drozdowski, K. Brylew, M. E. Witkowski, A. J. Wojtowicz, P. Solarz, K. Kamada and A. Yoshikawa, Studies of light yield as a function of temperature and low temperature thermoluminescence of $Gd_3Al_2Ga_3O_{12}$:Ce scintillator crystals, *Opt. Mater.*, 2014, **36**, 1665–1669.

19 Y. Wu, F. Meng, Q. Li, M. Koschan and C. L. Melcher, Role of Ce^{4+} in the scintillation mechanism of Ca^{2+}-codoped $Gd_3Ga_3Al_2O_{12}$:Ce, *Phys. Rev. Appl.*, 2014, **2**, 044009.

20 C. Wang, Y. Wu, D. Ding, H. Li, X. Chen, J. Shi and G. Ren, Optical and scintillation properties of Ce-doped $(Gd_2Y)Ga_{2.7}Al_{2.3}O_{12}$ single crystal grown by Czochralski method, *Nucl. Instrum. Methods Phys. Res., Sect. A*, 2016, **820**, 8–13.

21 M. T. Lucchini, V. Babin, P. Bohacek, S. Gundacker, K. Kamada, M. Nikl, A. Petrosyan, A. Yoshikawa and E. Auffray, Effect of Mg^{2+} ions co-doping on timing performance and radiation tolerance of cerium doped $Gd_3Al_2Ga_3O_{12}$ crystals, *Nucl. Instrum. Methods Phys. Res., Sect. A*, 2016, **816**, 176–183.

22 M. Korzhik, V. Alenkov, O. Buzanov, G. Dosovitskiy, A. Fedorov, D. Kozlov, V. Mechinsky, S. Nargelas, G. Tamulaitis and A. Vaitkevičius, Engineering of a new single-crystal multi-ionic fast and high-light-yield scintillation material $(Gd_{0.5}Y_{0.5})_3Al_2Ga_3O_{12}$:Ce,Mg, *CrystEngComm*, 2020, **22**, 2502–2506.

23 G. Dantelle, G. Boulon, Y. Guyot, D. Testemale, M. Guzik, S. Kurosawa, K. Kamada and A. Yoshikawa, Research on efficient fast scintillators: evidence and X-ray absorption near edge spectroscopy characterization of Ce^{4+} in Ce^{3+}, Mg^{2+}-codoped $Gd_3Al_2Ga_3O_{12}$ garnet crystal, *Phys. Status Solidi B*, 2020, **257**, 1900510.

24 P. Schauer, O. Lalinsky, M. Kucera, Z. Lucenicova and M. Hanus, Effect of Mg co-doping on cathodoluminescence properties of LuGAGG:Ce single crystalline garnet films, *Opt. Mater.*, 2017, **72**, 359–366.

25 S. Nargelas, Y. Talochka, A. Vaitkevičius, G. Dosovitskiy, O. Buzanov, A. Vasil'ev, T. Malinauskas, M. Korzhik and G. Tamulaitis, Influence of matrix composition and its fluctuations on excitation relaxation and emission spectrum of Ce ions in $(Gd_xY_{1-x})_3Al_2Ga_3O_{12}$: Ce scintillators, *J. Lumin.*, 2022, **242**, 118590.

26 M. Kitaura, H. Zen, K. Kamada, S. Kurosawa, S. Watanabe, A. Ohnishi and K. Hara, Visualizing hidden electron trap levels in $Gd_3Al_2Ga_3O_{12}$:Ce crystals using a mid-infrared free-electron laser, *Appl. Phys. Lett.*, 2018, **112**, 031112.

27 J. Bárta, K. S. Pestovich, J. A. Valdez, B. W. Wiggins, C. Richards, E. Smith, J. H. Clayton, D. Smalley and K. J. McClellan, Compositional screening of Ce-doped $(Gd,Lu,Y)_3(Al,Ga)_5O_{12}$ ceramics prepared by quenching from melt and their luminescence properties, *J. Alloys Compd.*, 2021, **889**, 161687.

28 V. Khanin, I. Venevtsev, K. Chernenko, V. Pankratov, K. Klementiev, T. van Swieten, A. J. van Bunningen, I. Vrubel, R. Shendrik, C. Ronda, P. Rodnyi and A. Meijerink, Exciton interaction with Ce^{3+} and Ce^{4+} ions in $(Lu,Gd)_3(Ga, Al)5O_{12}$ ceramics, *J. Lumin.*, 2021, **237**, 118150.

29 V. Pankratova, A. P. Kozlova, O. A. Buzanov, K. Chernenko, R. Shendrik, A. Šarakovskis and V. Pankratov, Time-resolved luminescence and excitation spectroscopy of Co-doped $Gd_3Ga_3Al_2O_{12}$ scintillating crystals, *Sci. Rep.*, 2020, **10**, 20388.

30 V. Babin, P. Bohacek, K. Jurek, M. Kučera, M. Nikl and S. Zazubovich, Dependence of Ce^{3+} – related photo- and thermally stimulated luminescence characteristics on Mg^{2+} content in single crystals and epitaxial films of $Gd_3(Ga,Al)5O_{12}$:Ce,Mg, *Opt. Mater.*, 2018, **83**, 290–299.

31 V. Babin, P. Herman, M. Kucera, M. Nikl and S. Zazubovich, Effect of Mg^{2+} co-doping on the photo- and thermally stimulated luminescence of the $(Lu,Gd)_3(Ga,Al)_5O_{12}$:Ce epitaxial films, *J. Lumin.*, 2019, **215**, 116608.

32 CMS Collaboration, A MIP Timing Detector for the CMS Phase 2 Upgrade, CERN-LHCC-2019-003.

33 LHCb Collaboration, Framework TDR for the LHCb Upgrade II, CERN-LHCC-2021-012.

34 L. Martinazzoli, N. Kratochwil, S. Gundacker and E. Auffray, Scintillation properties and timing performance of state-of-the-art $Gd_3Al_2Ga_3O_{12}$ single crystals'', *Nucl. Instrum. Methods Phys. Res., Sect. A*, 2021, **1000**, 165231.

35 V. Alenkov, O. Buzanov, G. Dosovitskiy, V. Egorychev, A. Fedorov, A. Golutvin, Y. Guz, R. Jacobsson, M. Korjik, D. Kozlov, V. Mechinsky, A. Schopper, A. Semennikov, P. Shatalov and E. Shmanin, Irradiation studies of a multi-doped $Gd_3Al_2Ga_3O_{12}$ scintillator, *Nucl. Instrum. Methods Phys. Res., Sect. A*, 2019, **916**, 226–229.

36 R. Y. Zhu, A Very Compact Crystal Shashlik Electromagnetic Calorimeter for Future HEP Experiments, *J. Phys.: Conf. Ser.*, 2017, **928**, 012015.

37 C. Hu, L. Zhang, R. Y. Zhu, M. Demarteau, R. Wagner, L. Xia, J. Xie, X. Li, Z. Wang, Y. Shih and T. Smith, Ultrafast inorganic scintillator-based front imager for Gigahertz Hard X-ray Imaging, *Nucl. Instrum. Methods Phys. Res., Sect. A*, 2019, **940**, 223–229.

38 K. B. Ucer, G. Bizarri, A. Burger, A. Gektin, L. Trefilova and R. T. Williams, Electron thermalization and trapping rates in pure and doped alkali and alkaline-earth iodide crystals studied by picosecond optical absorption, *Phys. Rev. B: Condens. Matter Mater. Phys.*, 2014, **89**, 165112.

39 M. T. Lucchini, O. Buganov, E. Auffray, P. Bohacek, M. Korjik, D. Kozlov, S. Nargelas, M. Nikl, S. Tikhomirov, G. Tamulaitis, A. Vaitkevicius, K. Kamada and A. Yoshikawa, Measurement of non-equilibrium carriers dynamics in Ce-doped YAG, LuAG and GAGG crystals with and without Mg-codoping, *J. Lumin.*, 2018, **194**, 1–7.

40 G. Tamulatis, G. Dosovitskiy, A. Gola, M. Korjik, A. Mazzi, S. Nargelas, P. Sokolov and A. Vaitkevicius, Improvement of response time in GAGG: Ce scintillation crystals by magnesium codoping, *J. Appl. Phys.*, 2018, **124**, 215907.

41 O. Sidletskiy, Ia Gerasymov, D. Kurtsev, V. Kononets, V. Pedash, O. Zelenskaya, V. Tarasov, A. Gektin, B. Grinyov, K. Lebbou, E. Auffray, V. Dormenev, A. Borisevich and M. Korjik, Engineering of bulk and fiber-shaped YAGG:Ce, *CrystEngComm*, 2017, **19**, 1001–1007.

42 S. Gundacker, E. Auffray, B. Frisch, P. Jarron, A. Knapitsch, T. Meyer, M. Pizzichemi and P. Lecoq, Time of flight positron emission tomography towards 100ps resolution with L(Y)SO: An experimental and theoretical analysis, *J. Instrum.*, 2013, **8**, P07014.

43 S. Gundacker, R. M. Turtos, E. Auffray and P. Lecoq, Precise rise and decay time measurements of inorganic scintillators by means of X-ray and 511 keV excitation, *Nucl. Instrum. Methods Phys. Res., Sect. A*, 2018, **891**, 42–52.

44 S. Gundacker, E. Auffray, K. Pauwels and P. Lecoq, Measurement of intrinsic rise times for various L(Y)SO and LuAG scintillators with a general study of prompt photons to achieve 10 ps in TOF-PET, *Phys. Med. Biol.*, 2016, **61**, 2802–2837.

45 G. Tamulaitis, A. Vasil'ev, M. Korzhik, A. Mazzi, A. Gola, S. Nargelas, A. Vaitkevičius, A. Fedorov and D. Kozlov, Improvement of the Time Resolution of Radiation Detectors Based on $Gd_3Al_2Ga_3O_{12}$ Scintillators With SiPM Readout, *IEEE Trans. Nucl. Sci.*, 2019, **66**, 1879–1888.

46 G. Tamulaitis, A. Vaitkevičius, S. Nargelas and R. Augulis, Subpicosecond luminescence rise time in magnesium codoped GAGG:Ce scintillator, *Nucl. Instrum. Methods Phys. Res., Sect. A*, 2017, **870**, 25–29.

47 G. Bizarri, W. W. Moses, J. Singh, A. N. Vasil'ev and R. T. Williams, An analytical model of nonproportional scintillator light yield in terms of recombination rates, *J. Appl. Phys.*, 2009, **105**, 044507.

48 M. Kirm, V. Nagirnyi, E. Feldbach, M. De Grazia, B. Carré, H. Merdji, S. Guizard, G. Geoffroy, J. Gaudin, N. Fedorov, P. Martin, A. Vasil'ev and A. Belsky, Exciton-exciton interactions in $CdWO_4$ irradiated by intense femtosecond vacuum ultraviolet pulses, *Phys. Rev. B: Condens. Matter Mater. Phys.*, 2009, **79**, 233103.

49 A. Gektin and A. Vasil'ev, Scintillator energy resolution and a way to improve it by kinetic waveform analysis, *Radiat. Meas.*, 2019, **122**, 108–114.

50 S. Vinogradov, Approximations of coincidence time resolution models of scintillator detectors with leading edge discrimination, *Nucl. Instrum. Methods Phys. Res., Sect. A*, 2018, **912**, 149–153.

51 S. Gundacker, R. M. Turtos, N. Kratochwil, R. H. Pots, M. Paganoni, P. Lecoq and E. Auffray, Experimental time resolution limits of modern SiPMs and TOF-PET detectors exploring different scintillators and Cherenkov emission, *Phys. Med. Biol.*, 2020, **65**, 025001.